

# Optic Flow Estimation on Trajectories Generated by Bio-Inspired Closed-Loop Flight

Patrick A. Shoemaker<sup>1</sup>, Andrew M. Hyslop<sup>2,3</sup>, J. Sean Humbert<sup>2</sup>

<sup>1</sup>Tanner Research, Inc., 825 South Myrtle Ave., Monrovia CA 91016, USA

<sup>2</sup>Department of Aerospace Engineering, University of Maryland, College Park MD 20742, USA

<sup>3</sup>Present affiliation: Emergent Space Technologies, 6301 Ivy Lane, Suite 720, Greenbelt MD 20770, USA

**Abstract.** We generated panoramic imagery by simulating a fly-like robot carrying an imaging sensor, moving in free flight through a virtual arena bounded by walls and containing obstructions. Flight was conducted under closed-loop control by a bio-inspired algorithm for visual guidance, with feedback signals corresponding to the true optic flow that would be induced on an imager (computed by known kinematics and position of the robot relative to the environment). The robot had dynamics representative of a housefly-sized organism, although simplified to two-degree-of-freedom flight in order to generate uniaxial (azimuthal) optic flow on the retina in the plane of travel. Surfaces in the environment contained images of natural and man-made scenes that were captured by the moving sensor. Two bio-inspired motion detection algorithms and two computational optic flow estimation algorithms were applied to sequences of image data, and their performance as optic flow estimators was evaluated by estimating the mutual information between outputs and true optic flow in an equatorial section of the visual field. Mutual information for individual estimators at particular locations within the visual field was surprisingly low (less than 1 bit in all cases) and considerably poorer for the bio-inspired algorithms than the man-made computational algorithms. However, mutual information between weighted sums of these signals and comparable sums of the true optic flow showed significant increases for the bio-inspired algorithms, whereas such improvement did not occur for the computational algorithms. Such summation is representative of the spatial integration performed by wide-field motion-sensitive neurons in the third optic ganglia of flies.

**Keywords.** Optic flow; visual guidance; elementary motion detector; fly vision; autonomous flight

**This is the web version of an article appearing in *Biological Cybernetics*:**

Shoemaker, Patrick A., Hyslop, Andrew M., and Humbert, J. Sean. Optic Flow Estimation on Trajectories Generated by Bio-Inspired Closed-Loop Flight. *Biological Cybernetics*, Vol. 104, No. 4, pp. 339-350; doi: 10.1007/s00422-011-0436-8, 2011.

**The original publication is available at:**

<http://www.springerlink.com/content/g500131132x7735k/fulltext.pdf>

## Introduction

### 1.1 Visual motion detection in insects and its role in flight control

Flying insects are able to navigate effectively using their low-resolution vision for pathfinding and obstacle avoidance (Borst and Haag, 2002; Egelhaaf et al., 2002; Srinivasan and Zhang, 2004). Some of the dipterans (true flies) rank among the most adept fliers in nature, able to avoid obstacles and moving objects such as predators effortlessly, while flying through cluttered environments. The tiny interocular separation in these animals precludes a significant role for stereopsis in this behavior. Based on these facts, we regard it as *axiomatic* that they must extract sufficient information about *optic flow* to enable reliable judgments about relation to objects in the environment when relative motion is occurring. By optic flow – more properly, ‘true’ optic flow – we mean the velocity field of the projection of material points in the viewing environment onto the retina, where those points form the surfaces of reflective (or possibly emissive) objects (Koenderink and van Doorn, 1987). The true optic flow field represents all that can be known from vision alone about relative motion between visual sensor and viewed environment. Of course, optic flow cannot be measured directly (and may not be measurable at all), but rather must be estimated based on spatiotemporal patterns of luminance on a retina. Such estimation may be limited by factors ranging from the presence or lack of incident illumination, of contrast in the visual imagery, to the properties of the optics associated with the sensor, the limitations of phototransduction, and limitations of the processing applied to visual signals.

Neurophysiological in addition to behavioral evidence has been found for visual motion detection in insects. In particular, the lobula plate tangential cells (LPTCs) in the dipterans have been the subject of electrophysiological study since the early 1980s (Hausen, 1982a, 1982b). These are large, motion-sensitive neurons with correspondingly broad receptive fields in visual space, and they are thought to integrate local motion cues over these receptive fields (Egelhaaf et al., 1989; Franceschini et al., 1989; Krapp et al., 1998). They project via interneurons to the flight control centers of the brain (Hausen, 1982a; Hausen and Egelhaaf, 1989).

Models have been developed for how visual motion detection is accomplished in the insect brain, based on both the behavioral and physiological evidence. One of the earliest but still most influential is the correlational *elementary motion detector* (EMD), which was formulated by Hassenstein and Reichardt (1956) on the basis of behavioral experiments. The outputs of local and retinotopically-distributed EMDs are assumed to form the inputs to LPTCs, and the response characteristics of the correlational EMD model have been found to be consistent with some of the significant electrophysiological characteristics of these neurons (see, e.g., Egelhaaf and Borst, 1993; Borst et al., 2010). The correlational EMD is one of a class of ‘motion energy’ detectors (Adelson and Bergen, 1985). Its fundamental operation is the *correlation* of a signal associated with one visual input unit with a delayed signal from a neighboring unit. Fig.1 depicts the EMD as implemented in the study. In this configuration, it may unambiguously be associated with the central early vision input, and its output is in synchrony with the optic flow in the viewing direction of that central photoreceptor.

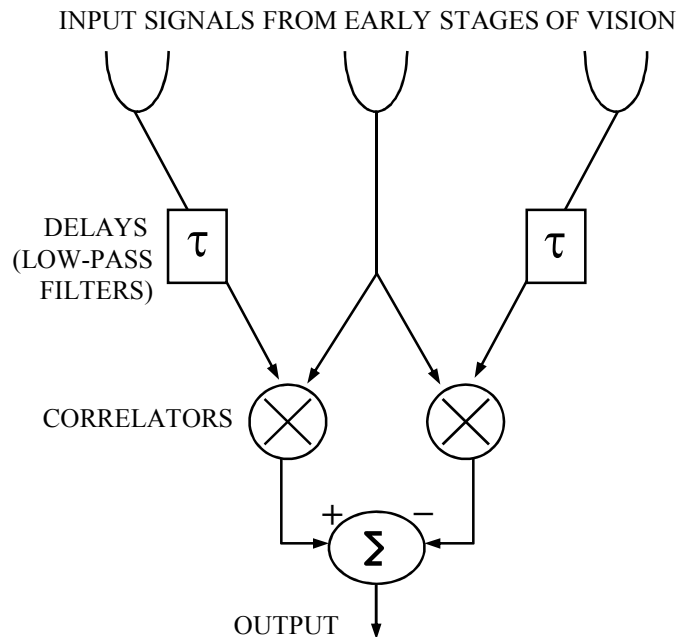


**Fig. 1.** The Hassenstein-Reichardt or correlational elementary motion detector, as implemented in this study. Inputs are from adjacent or nearby ommatidia in retinotopic space. This example gives a positive output for left-to-right motion: the output of the left correlator is in the mean greater than the output of the right correlator for such motion.

The delay is often implemented as the phase delay of a temporal lowpass filter. The final opponent stage in Fig. 1, which takes the difference of two mirror-image correlator outputs, enhances the directional properties and rejection of temporal contrast not due to motion. The correlational EMD produces a motion-related output without computing derivatives (a process that would amplify noise).

Although the predictions of this model are consistent with a number of behavioral and electrophysiological results, in isolation it is an ambiguous motion sensor and of questionable value for estimation of optic flow. Its output in response to a moving visual scene is typically unsteady, with transients generated in response to the passage of edges or contrast gradients. In the *mean*, the output is a function of velocity of a moving stimulus, although this dependence is not monotonic. In addition, it has a strong dependence on spatial structure and contrast of the stimulus. These shortcomings, as well as the results of additional behavioral experiments that appear inconsistent with model predictions, have led some to postulate that other mechanisms of motion detection may operate in parallel or in competition in the insect brain (Srinivasan et al., 1993). Despite this, the bulk of the evidence strongly suggests insects (as well as many other animals) use similar EMDs as the basis for optical flow analysis (van Santen and Sperling, 1984; Egelhaaf et al., 1989; Wolf-Oberhollenzer and Kirschfeld, 1994; Clifford and Ibbotson, 2003; Haag et al., 2004).

In contrast with the dependence of EMD model outputs on scene contrast and structure, experimental evidence shows that LPTCs display ‘velocity constancy’ – that is, remarkably consistent velocity tuning properties over a variety of moving natural

imagery (Straw et al., 2008; Barnett et al., 2010). Furthermore, several factors contributing to this consistency have been identified. One is the fact that natural scenes (and even a wide variety of man-made ones) tend to have consistent, broadband spatial statistics (Tolhurst et al., 1992; Dror et al., 2001). Also playing a significant role are the nonlinear and adaptive features of the processing pathway. One such feature is motion adaptation (Maddess and Laughlin, 1985; Clifford and Langley, 1996; Harris et al., 2000), a reduction in sensitivity seen after the system is exposed to moving imagery. This is due largely to a reduction in gain in the prior signal processing pathway (Harris et al., 1999; Harris et al., 2000), and is spatially local (i.e., occurring prior to integration of motion detector outputs) (Harris et al., 2000). Modeling results suggest that adaptation, along with other nonlinearities in the processing pathway, can significantly reduce the contrast dependence of the correlational EMD and thus may play a role in consistent velocity sensing by the tangential cells (Shoemaker et al., 2005).

## 1.2 Context and methods of comparative study

It is the intention of this study to evaluate the quality of optic flow estimation by the correlational EMD model, expanding on the work reported in Shoemaker et al. (2005) and comparing results from the EMD to optic flow estimation by several other man-made algorithmic techniques. In order to generate optic flow with realistic statistics, simulations were run in which a vision sensor was attached to a robotic agent that moved through a virtual environment according to a closed-loop control algorithm that is inspired by the neurophysiology and flight control of the fly (Humbert et al., 2010; Hyslop et al., 2010). This algorithm accepts optic flow (or an estimate) as input, and produces characteristic responses that reflect a number of the navigational heuristics seen in flying insects (in particular, the honeybee (Srinivasan et al., 1996)). In this study, the feedback input to the control algorithm was the *true* optic flow relative to the vantage point of the vision sensor, computed from its motion and spatial relationship to objects in the virtual environment. Actuation commands were generated, and corresponding forces applied to the agent – a ‘flybot’ with fly-like dynamics – to close the loop. Although true optic flow was used for control purposes, optic flow estimates based strictly on visual data were also computed and stored. These were compared with the true optic flow using a statistical metric, in order to evaluate the estimating power of the visual motion detection models.

## 2 Model

### 2.1 Virtual Environment

The ‘flybot’ agent is embedded in a virtual environment comprising a flight arena with obstacles. The ‘flybot’ is constrained to travel within a horizontal plane in this environment, but it views three-dimensional surroundings. The arena is a 4m cube, and the obstacles are vertical pillars of square cross-section. Four of these are 0.5m on a side and eight are 0.25m on a side in cross-section. Pillars are placed randomly on a 0.25m grid, subject to an exclusion constraint that requires a horizontal distance of at least the pillar width to walls or other pillars of equal or larger size. Imagery containing natural and man-made objects is attached to the internal walls of the arena and the sides of the

pillars, to endow them with broadband spatial statistics when viewed. A depiction of this virtual flight arena is shown in Fig. 2.

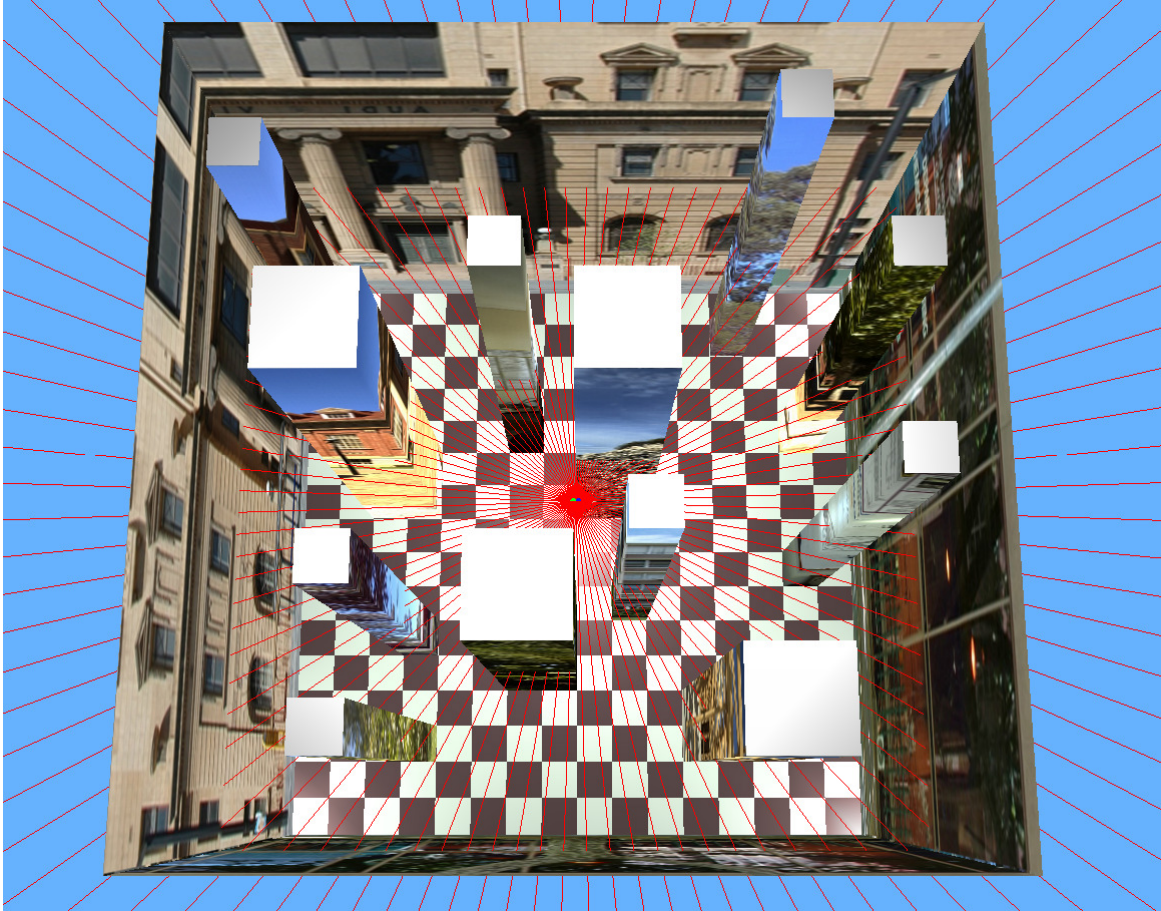


**Fig. 2.** Virtual flight arena as implemented in the robotics simulation program Webots. The ‘flybot’ is at center; the red lines indicate the central lines of sight of its simulated photodetectors, as well as the rays of its distance sensors.

## 2.2 Kinematics and Dynamics

The dynamical model for the ‘flybot’ is intended to be roughly representative of a housefly, although with simplified dynamics and kinematics. We treat the ‘flybot’ as a rigid body and in addition to restricting its motion to a plane, we preclude roll and pitch rotations, leaving two degrees of translational and one degree of rotational (i.e., yaw rotation) freedom. Although it is clear that flies can undergo sideslip during aerobatic maneuvers (Collett and Land, 1975), for this study we also made a simplifying assumption of *coordinated flight*, i.e., that centripetal aerodynamic forces are applied by the ‘flybot’ during turns to prevent sideslip, such that its velocity and heading vectors are at all times in the same direction. With this constraint, the degrees of freedom of the dynamics are reduced to two in number, in particular the forward or tangential velocity  $v$  and angular velocity  $\omega$  about the vertical or yaw axis. The  $x$  and  $y$  components of velocity in a Cartesian frame of reference attached to the environment become  $v_x = v \cos(\phi)$  and  $v_y$ ,

$= v \cdot \sin(\phi)$  respectively, where  $\phi = \int \omega dt$  indicates orientation angle with respect to that frame of reference.

Dynamical parameters are chosen to be representative of animals the size of *Musca* or *Calliphora*, but based primarily on the more extensive literature for *Drosophila* (Fry et al., 2003; Reiser et al., 2004; Hesselberg and Lehmann, 2007; Dickson et al., 2008) with appropriate rescaling according to dynamic scaling principles. For this purpose the ‘flybot’ is assumed to be 2.5 times as large as *Drosophila* in linear scale. Translational and rotational dynamics are assumed to be uncoupled. For the rotational damping coefficient of a fruit fly in flight, we chose a value between lower estimates based on body morphology and Stokes’ law (Fry et al., 2003) and higher estimates that take into account viscous effects due to the wing beats (Hesselberg and Lehmann, 2007). In Table 1 is a summary of the parameters and the associated generalized forces:

Parameter	Symbol	Value	Generalized Force
Mass	$M$	$1.56 \cdot 10^{-5} \text{kg}$	$M \cdot a$
Translational damping coefficient	$D$	$3.1 \cdot 10^{-6} \text{Nm}^{-2} \text{s}^2$	$-D \cdot v^2 \cdot \text{sgn}(v)$
Moment of inertia	$J$	$5.1 \cdot 10^{-11} \text{kg} \cdot \text{m}^2$	$J \cdot \alpha$
Rotational damping coefficient	$C$	$3.2 \cdot 10^{-10} \text{Nms}$	$-C \cdot \omega$

**Table 1.** Dynamic parameters characterizing the ‘flybot’.

In the final column of Table 1,  $a$  is linear acceleration  $dv/dt$ ,  $\alpha$  is angular acceleration  $d\omega/dt$ , and  $\text{sgn}(\ast)$  indicates algebraic sign. These forces are balanced by actuation forces corresponding to forward thrust and torque.

### 2.3 Sensing

Although the ‘flybot’ moves in a plane, this plane is embedded in a three-dimensional virtual flight arena for purposes of visual sensing. For the EMD-based optic flow estimators, as well as the Gradient Method defined below in Section 2.4.2.1, the visual sensor comprises four rings of 96 ‘photodetectors’, each viewing a panorama about the vertical axis. An individual detector subtends a viewing angle of  $3.75^\circ$  in azimuth and elevation, and is intended to correspond to an ommatidium of a compound eye. It is monochromatic, operating on green channel data from the color imagery in order to approximate the spectral sensitivity of the receptors used for motion vision in the fly (Srinivasan and Guy, 1990). The viewing angles of the detector rings are distributed symmetrically in elevation about the horizontal plane, but with an empty or unviewed ring of vertical extent  $3.75^\circ$  between any two successive sensor rings to reduce the correlation between the imagery viewed by each. For a second numerical method, the Lucas-Kanade algorithm detailed in Section 2.4.2.2 below, the imagery in these same rings is sampled at three times the linear resolution of the model ‘photodetectors’, although optic flow estimates are rendered at the same 96 locations on each ring.

In addition to visual sensing, the ‘flybot’ is equipped with a ring of 96 distance sensors that measure horizontal distances to 96 points on solid objects in the virtual environment. These distance sensors are aligned with the azimuthal viewing angles of the detector centroids in the visual sensor, and are used to compute true optic flow at each location.

All sensors are treated as infinitesimal in size.

## 2.4 True and Estimated Optic Flow

Under the specified kinematic constraints, it is the horizontal view that is relevant to the local guidance and obstacle avoidance problem, and the optic flow on the corresponding circle on the visual sphere is purely circumferential in direction. Accordingly, the architectures of the sensing and processing systems are set up to measure or estimate circumferential component of optic flow at points around the horizon, as defined by the viewing angles of the visual detectors and distance sensors.

In order to compute the true optic flow on this circle, the sensed horizontal distances at each of the 96 azimuthal angles is used along with the known kinematic state of the ‘flybot’. Azimuthal viewing angle  $\gamma$  is specified relative to the forward direction for the ‘flybot’ with sense determined by the right-hand rule relative to the vertical axis. With this convention, the circumferential optic flow  $\dot{q}_\gamma \equiv dq_\gamma / dt$  in the direction of increasing  $\gamma$  is given by

$$\dot{q}_\gamma = -\omega + \mu_0(\gamma) \cdot v \sin(\gamma), \quad (1)$$

where  $dq_\gamma$  is local infinitesimal angular displacement of the image in the  $\gamma$ -direction, and where  $\mu_0$  is the inverse of the horizontal distance to an object in the environment at the viewing angle  $\gamma$ , as depicted in Fig. 3.

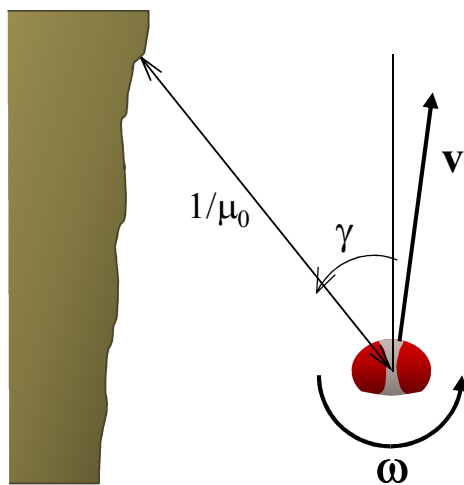


**Fig. 3.** Convention for the geometric and kinematic quantities that determine the circumferential optic flow, in a plan view looking down on the vision sensor. In a body-referred frame, azimuthal line-of-sight angle  $\gamma$  is defined relative to the frontal direction, with sense given by the right-hand rule relative to the vertical axis. The horizontal distance to an object in the environment at viewing angle  $\gamma$  is  $1/\mu_0(\gamma)$ . Translational velocity  $\mathbf{v}$  and angular velocity  $\omega$  induce optic flow  $\dot{q}_\gamma$  on the retina, taken as positive in the direction of increasing  $\gamma$ .

The use of multiple visual sensor rings at several elevations about the horizon allows the formation of multiple estimates of the circumferential component of optic flow, but also introduces some error when translational motion is present, since the true optic flow at these non-zero elevations is not identical to that in the horizontal plane. We bound this error as follows. Equation (1) remains valid for non-equatorial rings if  $\mu_0(\gamma)$  is replaced

by the inverse of the line-of-sight distance to an object in the environment in the direction of the normal to the visual sphere,  $\mu(\gamma, \beta)$ , where  $\beta$  indicates elevation angle relative to the horizontal. Because the viewed surfaces of all objects in the ‘flybot’ arena are vertical, the  $\beta$  dependence of  $\mu(\gamma, \beta)$  is straightforward:  $\mu(\gamma, \beta) = \cos(\beta) \mu_0(\gamma)$ . Thus, a cosine error is introduced by the use of non-equatorial rings of sensors in the estimation of circumferential optic flow in the horizontal plane. For the centroids of the uppermost and lowermost rings,  $\beta = \pm 11.25^\circ$ , respectively, and  $\cos(\beta) = 0.981$ . Because the resultant error is less than 2% in relative terms, and in general is considerably smaller than estimation errors, we ignore its effects in our evaluation of estimator quality.

#### 2.4.1 Estimation by Bio-Inspired Visual Motion Detection

In our bio-inspired motion detection models, the intensity signal from each detector serves as input to a visual processing unit that provides a rough approximation to the characteristics of the insect photoreceptors and early vision. Photoreceptor nonlinearity is modeled by a Lipetz (1971), or Naka-Rushton (Naka and Rushton, 1966) transformation, specified by the equation

$$U = I^a / (I^a + I_0^a),$$

where  $I$  is the input intensity,  $I_0$  a parameter defining mid-response level,  $a$  is a fractional exponent that is set to the value 0.7, and  $U$  is the output. This equation gives log-linearity of response over roughly a decade of intensities about the mid-response level. Photoreceptor adaptation is modeled by setting the mid-level parameter  $I_0$  to a temporal average of the input intensity, as computed with a first-order lowpass filter with transfer function (Laplace transform)  $1/(\tau_L s + 1)$ , where  $s$  is the Laplace variable, and the time constant  $\tau_L$  is set to 1.2s.

Following this transform, a first-order temporal highpass filter with transfer function  $\tau_H s / (\tau_H s + 1)$  and time constant  $\tau_H = 120\text{ms}$  is applied to remove the dc component of each photoreceptor output signal, and to serve as an approximation of the transient characteristics of neurons in the first optic ganglion, such as the Lamina Monopolar Cells (LMCs) (Laughlin, 1976, 1984). The outputs of this filter stage are regarded as the inputs to the subsequent motion detection stage.

Motion detection is based on the correlational elementary motion detector in the architecture depicted in Fig. 1. The delay operator is implemented as the phase delay of a first-order temporal lowpass filter with a time constant  $\tau_D$  of 21ms, leading to a velocity tuning curve (the function relating mean EMD output to optic flow velocity) with an optimum (i.e., argmax) at about  $175^\circ\text{s}^{-1}$  for natural imagery, consistent with the velocity tuning of larger flies such as *Eristalis tenax* (Straw et al., 2008). The correlator in the EMD is implemented as a multiplier. In our model, EMDs are formed between azimuthally adjacent visual processing units within each sensor ring.

In addition to an EMD that operates directly on early visual output (the ‘Raw EMD’), two additional models with motion adaptation were included. Motion adaptation took the form of local gain control applied to individual early vision outputs. In one version (the ‘EMD with Gain Control’), the mean absolute deviation (MAD) of each individual early vision output signal was estimated by full-wave rectification followed by a linear, first-order temporal lowpass filter (transfer function  $1/(\tau_A s + 1)$ ), with time constant  $\tau_A$

assigned the value 200ms. The early vision signal was then divided by the MAD estimate. In a second version (the ‘EMD with Neural Gain Control’), a model for shunting inhibition driven by the MAD estimate was employed, with the output  $Out$  taking the form

$$Out = In / (|In| + MAD(In) + \varepsilon) ,$$

where  $In$  indicates input,  $MAD(In)$  the MAD estimate, and  $\varepsilon$  a small constant (corresponding to resting membrane conductance in a neural compartment) that was assigned the value 0.05. This ‘neural’ gain control more tightly constrains the magnitudes of output variations than the non-neural version. In either case, the time constant  $\tau_A$  is a measure of the characteristic time scale of adaptation. These gain control models are similar to the approach of Kirschfeld (1991) except for the point of application of the variable gain.

## 2.4.2 Other Optic Flow Estimation Methods

### 2.4.2.1 One-Dimensional Gradient Method

The so-called *gradient method* is based on a continuity constraint for image intensity, along with an assumption of constant intensity at any material point in the environment. The general optic flow on a two-dimensional imaging surface is underdetermined by this continuity equation. However, because we consider only uniaxial optic flow in the  $\gamma$ -direction, the constraint can be solved directly for the flow based on the one-dimensional spatial and the temporal gradients:

$$\frac{\partial I}{\partial \gamma} dq_\gamma + \frac{\partial I}{\partial t} dt = 0 \quad \therefore \quad \frac{dq_\gamma}{dt} = -\frac{\partial I / \partial t}{\partial I / \partial \gamma} , \quad (2)$$

where  $I$  is image intensity as a function of location (azimuth  $\gamma$ ) on the sensing surface and time  $t$ . This algorithm will be denoted simply the ‘Gradient Method’ in the remainder of the paper. In practice, numerical derivatives were estimated by averaging two non-centered finite differences, with a step size of one metapixel for the spatial derivative.

### 2.4.2.2 Basic Lucas-Kanade Algorithm

The algorithm developed by Lucas and Kanade (1981) was selected as the top-performing algorithm in a comprehensive performance comparison of optic flow estimation algorithms in closed-loop navigation tasks by McCarthy and Barnes (2004), and is regarded herein as a performance standard for that purpose. The Lucas-Kanade algorithm is designed to operate on two-dimensional pixel data and provide two-dimensional optic flow estimates. It solves the underdetermined continuity constraint equation by imposing an additional constraint of constant image velocity over a small window  $W$  consisting of sampling locations around the location of interest. In our analysis, each window subtends the same area as one ‘photodetector’ as defined for the other optic flow estimation methods, and has the same centroid. Nine samples of the image are taken in a 3x3 grid within each window, but a single optic flow estimate is produced for the entire window, corresponding to the motion of its central element. Numerical estimates of spatial derivatives are computed by centered finite differencing about each sample location. This configuration of the Lucas-Kanade algorithm thus

requires image data at nine times the resolution of the other methods, but as implemented, produces optic flow estimates at the same 96x4 locations.

The constraint generates an overdetermined set of linear equations that can be solved using a least-squares approach. The objective is to minimize the sum of squares of the constraint error at each window:

$$J = \sum_{(\gamma, \beta) \in W} \left( \frac{\partial I(\gamma, \beta; t)}{\partial \gamma} \cdot \dot{q}_\gamma + \frac{\partial I(\gamma, \beta; t)}{\partial \beta} \cdot \dot{q}_\beta + \frac{\partial I(\gamma, \beta; t)}{\partial t} \right)^2,$$

where  $I$  is a function of location (azimuth  $\gamma$  and elevation  $\beta$ ) on the sensing surface and time, and  $\dot{q}_\beta$  indicates the local vertical component of optic flow. The least-squares solution of the minimization problem is

$$\begin{bmatrix} \dot{q}_\gamma \\ \dot{q}_\beta \end{bmatrix} = \left( \sum_{(\gamma, \beta) \in W} \begin{bmatrix} (\partial I / \partial \gamma)^2 & \partial I / \partial \gamma \cdot \partial I / \partial \beta \\ \partial I / \partial \gamma \cdot \partial I / \partial \beta & (\partial I / \partial \beta)^2 \end{bmatrix} \right)^{-1} \left( \sum_{(\gamma, \beta) \in W} \begin{bmatrix} \partial I / \partial t \cdot \partial I / \partial \gamma \\ \partial I / \partial t \cdot \partial I / \partial \beta \end{bmatrix} \right)$$

In a discrete-time system, Newton-Raphson iteration is conducted for the inter-sample shift estimate (corresponding to the optic flow multiplied by the sample time), based on re-computation of the temporal gradients at the current estimate, until the cost function converges. The *OpenCV* implementation of this algorithm (Bouguet 1999) was used in this study, without pyramidal resolution iteration (a method allowing better estimates for large shifts, corresponding to high optic flow rates).

For purely uniaxial optic flow, a basic form of the Lucas-Kanade algorithm can still be applied in order to leverage Newton-Raphson iteration and window sizes larger than one. The estimated optic flow in this case becomes:

$$\dot{q}_\gamma = \left( \sum_{(\gamma, \beta) \in W} (\partial I / \partial \gamma)^2 \right)^{-1} \left( \sum_{(\gamma, \beta) \in W} \partial I / \partial t \cdot \partial I / \partial \gamma \right). \quad (3)$$

## 2.5 Flight Control Based on Wide-Field Integration

The reflexive navigation approach used to guide the ‘flybot’ through the environment is based on extracting relative proximity information by integrating local motion estimates across the field of view. Inspired by LPTC processing principles, the *matched filter* hypothesis (Franz et al., 2000; Dahmen et al., 2001) suggests an individual cell's output can be considered as a comparison between a cell's *directional template* (as implemented by the strengths of synaptic connections from individual EMDs onto the target LPTC) and the current pattern of optic flow. Mathematically, this comparison can be modeled as an inner product on a continuous spatial domain (Humbert et al., 2010), in our case defined for uniaxial, circumferential optic flow  $\dot{q}_\gamma$ :

$$C = \int_0^{2\pi} \dot{q}_\gamma(\gamma) F(\gamma) d\gamma,$$

where  $C$  is the matched filter output, and  $F(\gamma)$  is a square-integrable weighting function such that the above integral exists.

This information extraction approach has been previously analyzed in a control-theoretic context (Humbert et al., 2010; Hyslop et al., 2010), yielding weighting functions that provide estimates of rotational velocity ( $F = 1/(\sqrt{2}\pi)$ ), rotational proximity ( $F = \cos(\gamma)/\pi$ ), forward speed ( $F = \sin(\gamma)/\pi$ ), and relative lateral proximity ( $F = \cos(2\gamma)/\pi$ ), where proximities are defined in relation to straight-ahead, centerline travel through a

corridor, as a prototype for the collision avoidance problem. The resulting set of outputs ( $A0$ ,  $A1$ ,  $B1$ , and  $A2$ , respectively) are applied as feedback (Fig. 4) with appropriate gains to reflexively maneuver the agent through the environment shown in Fig. 2. The  $B1$  output controls forward thrust with a gain of  $-2.0 \cdot 10^{-6}$ Ns, and an offset of  $2.5 \cdot 10^{-5}$ N (to set the reference forward velocity for the ‘flybot’). The  $A0$ ,  $A1$ , and  $A2$  outputs control torque with gains of  $6.0 \cdot 10^{-9}$ Nms,  $-5.0 \cdot 10^{-8}$ Nms, and  $1.0 \cdot 10^{-7}$ Nms, respectively.

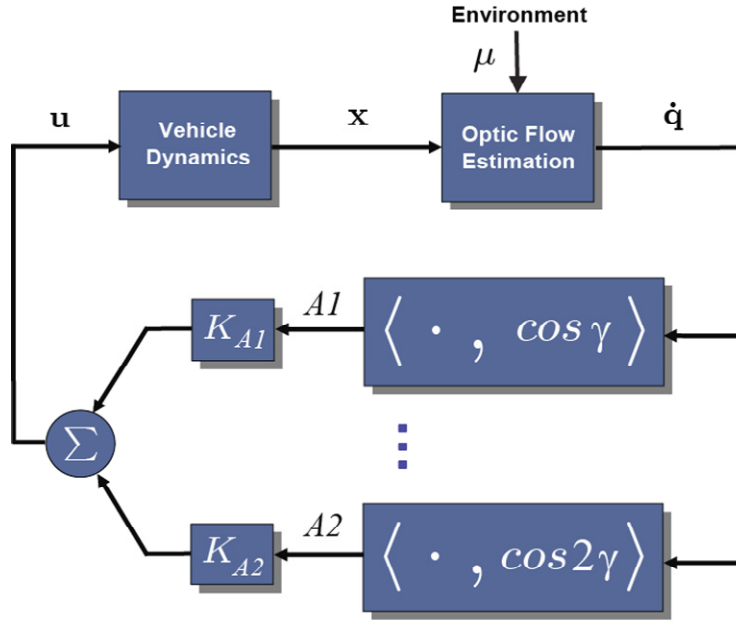


**Fig. 4.** Feedback architecture for Wide-Field Integration. Patterns of optic flow  $\dot{q}_\gamma$  are integrated against weighting functions (e.g.,  $F = \cos(\gamma)$ ) to generate outputs (e.g.,  $A1$ ) that contain velocity and proximity information. These outputs are subsequently applied as feedback with appropriate gains to generate reflexive navigation behavior.

The original WFI algorithm does not mitigate against head-on collision with symmetric objects dead ahead, nor against collisions with small objects that do not cause a significant disturbance in the overall optic flow field. In order to prevent such collisions and near-collisions, we augmented the WFI with a *looming detector*, inspired by a class of motion-sensitive neuron found in some insects such as the locust (Rind, 1996). Our looming detector is formulated by computing the second sine mode of the circumferential optic flow, with support over the front half of the visual field only (the corresponding basis function,  $\sin(2\gamma)/\pi$  for  $\gamma \in (-\pi/2, \pi/2)$ , matches the pattern of optic flow induced by perpendicular approach to an infinite surface). This quantity, referred to as  $B2_f$ , gives a positive input for approach to an obstacle, and in order to contribute to evasion of such an obstacle, it is used as a torque feedback term after modulation by a function that endows it with a sign in order to specify the direction to turn. To compose this modulating function, the algebraic sign of the first cosine mode,  $\text{sgn}(A1)$ , is passed through a first order temporal lowpass filter with time constant 50ms. The sign of the  $B2_f$  term thus follows that of the  $A1$  term but with a short lag that prevents oscillatory behavior. The term is multiplied by the same gain,  $-5.0 \cdot 10^{-8}$ Nms, as the gain for the  $A1$  feedback term,

and then added to the  $A0$ ,  $A1$ , and  $A2$  terms in order to form the complete torque control signal.

### 3 Simulation Environment

For this study, our simulation environment comprised a hybrid system using the simulation and numerical analysis package MATLAB / Simulink (the MathWorks, Natick, MA), and the robotics simulation program Webots (Cyberbotics, Lausanne, Switzerland). The virtual environment and sensors are implemented in Webots. The walls and pillars in the environment are defined by specifying geometrical objects with imagery attached to surfaces to provide the visual texture. Implementation of sensory processing, the control algorithms, and the robot dynamics is implemented in MATLAB / Simulink. The two programs communicate via a TCP/IP socket using a custom interface, and update each other incrementally as a simulation progresses. The simulation time increment between successive updates is 8ms. A complete MATLAB/Simulink simulation is run for each time step, with the visual data linearly interpolated between the current and previous values during the simulation in order to form the inputs. An updated location is subsequently passed from MATLAB back to Webots to allow repositioning of the ‘flybot’, and the acquisition of new visual data for the following time step.

Visual sensing is implemented by simulated cameras in Webots. Twelve separate cameras are used to form a panoramic image, in order to minimize projection distortion (which is modeled by the sensors). In Webots, the camera function is implemented by casting a ray in the viewing direction of each pixel in the sensor, and recovering the luminance at a point on the first solid reflective surface that the ray intersects, at each timestep. This scheme leaves the sensors susceptible to spatial undersampling when the imagery attached to environmental surfaces contains spatial frequency components higher than the Nyquist frequency for the sensor, which in this case means having periods less than twice the distance between the intersections of the sensor rays and environmental surfaces. This criterion depends on the distance and angle between the sensor plane and the viewed surface, as well as on the spatial spectrum of the imagery on the surface.

The following approach was taken to limit spatial undersampling. All images attached to surfaces in the flight arena are spatially band-limited, with raw imagery passed through a Lanczos lowpass filter before use in the arena. The camera resolution – 10.93 pixels per degree – and the corner frequency for the spatial filtering operation –  $41.25\text{m}^{-1}$  – are chosen such that undersampling of imagery on one wall of the arena is precluded when it is viewed from any position on the opposite wall. However, when the angle between the sensor and a surface in the arena is sufficiently oblique, it is impossible to preclude undersampling entirely; with the geometric, image, and sensing parameters as chosen, we calculate that undersampling cannot occur over areas greater than  $7^\circ$  in extent in their projections onto the sensor.

Raw pixel data from the camera elements are binned together into *metapixels*, which comprise the outputs of ‘photodetectors’ for purposes of motion vision. Except for the Lucas-Kanade algorithm, the linear oversampling ratio is 41, i.e., 1681 pixel values over a square area are summed to yield a metapixel value. This yields the stated 96 detectors per horizontal sensor ring. This sensing scheme provides a natural increase in absolute

resolution of the binned ‘retinal’ imagery relative to that of the surface image as an object is approached by the ‘flybot’, maintaining realistic spatial statistics over a range of distances varying by a factor of 41. For the Lucas-Kanade data, higher-resolution imagery is produced by downsampling the raw image data to three times the linear resolution of the metapixel data, as indicated in Section 2.4.2.2.

#### 4 Experimental Design and Data Analysis

The ‘flybot’ was allowed to navigate freely through the virtual flight arena using the augmented WFI algorithm for pathfinding. Ten separate simulations were performed from ten different initial positions and orientations throughout the arena, with each lasting for 16s of simulated time. Each 16 second segment was preceded by a 1.2 second segment of open-loop, straight-ahead flight, with a constant thrust scaled to induce a steady-state velocity of  $0.25\text{ms}^{-1}$ , in order to allow the time-dependent parts of the estimators to initialize. Initial conditions were chosen by trial and error in an effort to minimize the overlap of the generated paths. Lack of overlap is difficult to achieve because when the positions and orientations of the flybot become similar during the course of two different simulations, the subsequent paths tend to converge. The ten trajectories used to generate the data used for analysis are depicted in a plan view of the flight arena in Fig. 5.

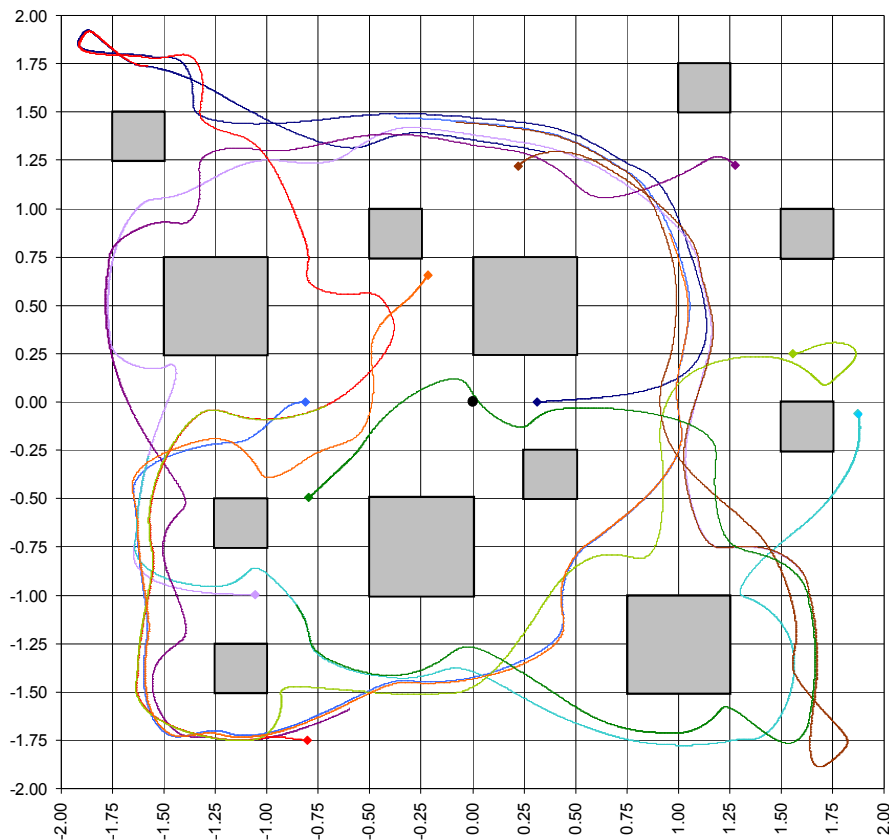


**Fig. 5.** Ten trajectories (colored curves) generated by simulations of the ‘flybot’ in free flight, depicted in a plan view of the virtual flight arena. A dot indicates the initial point of each trajectory. Pillar locations are indicated by gray squares, and scales indicate global coordinates in meters.

At each 8ms time step during each simulation, the true circumferential optic flow was computed and recorded at each of the 96 viewing angles, as well as the metapixel datum for each detector in the four rings. Subsequently, optic flow estimates for the various methods were computed based on the metapixel data. Several pilot experiments were run in which data were recorded every 4ms, with little effect on the results, and so it was concluded that temporal undersampling of the vision data during execution of the trajectories is of minor significance at the  $125\text{s}^{-1}$  sample rate.

Each of the four optic flow estimates at a particular viewing angle and time step is associated with the true optic flow at the same location and time, such that the experiment generated a total of  $7.68 \cdot 10^6$  joint occurrence data for each estimator. The quality of the optic flow estimates was evaluated using the mutual information between each estimator and true optic flow, treating the two as random variables. This metric is independent of the scaling of the estimator outputs, and its values are likewise not necessarily degraded by nonlinearity in the relationship between estimator mean and optic flow velocity, so long as that relationship is monotonic. The dependence of mean EMD output on velocity is, however, nonmonotonic, and when optic flow velocities beyond the velocity optimum are evoked during the trajectories, the result is necessarily a reduction in mutual information.

In addition to this evaluation of the estimators, a second analysis was carried out to provide a point of reference for the mutual information values obtained for them. In this analysis, zero-mean Gaussian random numbers were added to the true optic flow values, and mutual information between noisy and true optic flow data was computed. The process was repeated for several different standard deviations of the Gaussian noise. In each case, four sets of noisy data were produced so that each mutual information figure was based on  $7.68 \cdot 10^6$  joint occurrence data, to match the number obtained from the four sensor rings for each estimator. The standard deviations of the noise were scaled relative to the mean absolute value of the true optic flow rate computed over the entire set of data.

The mutual information M.I.(continuous) between true optic flow and a particular estimator may be written:

$$\text{M.I.}(\text{continuous}) = \int_x \int_y p[\text{OF}=x \cap \text{EST}=y] \cdot \log_2 \{ p[\text{OF}=x \cap \text{EST}=y] / (p[\text{OF}=x] \cdot p[\text{EST}=y]) \} dx dy,$$

where M.I.(continuous) is here measured in bits, OF indicates true optic flow and EST estimator output, the function  $p[\text{OF}=x \cap \text{EST}=y]$  is a joint probability density function,  $p[\text{OF}=x]$  and  $p[\text{EST}=y]$  are marginal probability density functions, and the integral is taken over all values of true optic flow and estimator outputs that would be generated by the closed-loop system in the given environment. In practice, mutual information is estimated by a quantity M.I.(discrete) based on empirical distributions obtained from the experiments, and computed using joint and marginal histograms for each optic flow estimator and true optic flow:

$$\text{M.I.}(\text{discrete}) = \sum_i \sum_j f[\text{OF} \in \text{bin}_i \cap \text{EST} \in \text{bin}_j] \cdot \log_2 \{ f[\text{OF} \in \text{bin}_i \cap \text{EST} \in \text{bin}_j] / (f[\text{OF} \in \text{bin}_i] \cdot f[\text{EST} \in \text{bin}_j]) \},$$

where  $f$  indicates relative frequency, and  $\text{bin}_i$  and  $\text{bin}_j$  refer to indexed bins in the marginal and joint histograms for OF and EST, respectively, that contain at least one

occurrence, with the quantity  $f [OF \in \text{bin}_i \cap EST \in \text{bin}_j]$  computed on the joint histogram over bins containing at least one occurrence. In the reference analysis, the estimator output values were replaced by the optic flow values contaminated with additive Gaussian noise.

In order to estimate M.I.(continuous) as accurately as possible, multiple histograms were constructed at different resolutions, and the corresponding M.I.(discrete) values, as well as the biases in these estimates, were computed and used in a procedure to derive the final figures presented below. This procedure is detailed in the Appendix.

In a similar analysis, the Fourier modes  $A0$ ,  $A1$ ,  $A2$ ,  $B1$ , and  $B2_f$  were computed at each time step for both the true optic flow and optic flow estimator, and the mutual information for each of these modes was estimated.

## 5 Results and Discussion

Results of the analysis of estimator performance are summarized in Table 2:

ESTIMATOR	SINGLE	$A0$	$A1$	$A2$	$B1$	$B2_f$
Raw EMD	0.0523	1.36	0.139	0.129	0.168	0.194
EMD w/ Gain Control	0.0653	1.21	0.110	0.106	0.174	0.191
EMD w/ 'Neural' Gain Control	0.0642	1.24	0.0918	0.0860	0.175	0.163
Gradient Method	0.402	0.361	0.0482	0.0503	0.0587	0.0743
Basic Lucas-Kanade	0.414	0.509	0.259	0.442	0.236	0.367

**Table 2.** Mutual information in bits between various optic flow estimators and true optic flow. 'SINGLE' indicates individual estimators, with the sample extending over all azimuthal viewing locations as well as time steps and trajectories, and containing  $7.68 \cdot 10^6$  joint occurrence data. The remaining columns give figures for the mutual information between the spatial Fourier modes of true optic flow and estimators, over all time steps and trajectories, corresponding to a sample with  $8 \cdot 10^4$  joint occurrence data.

Mutual information between true and noise-contaminated optic flow is shown in Fig. 6 as a function of the standard deviation of the noise.

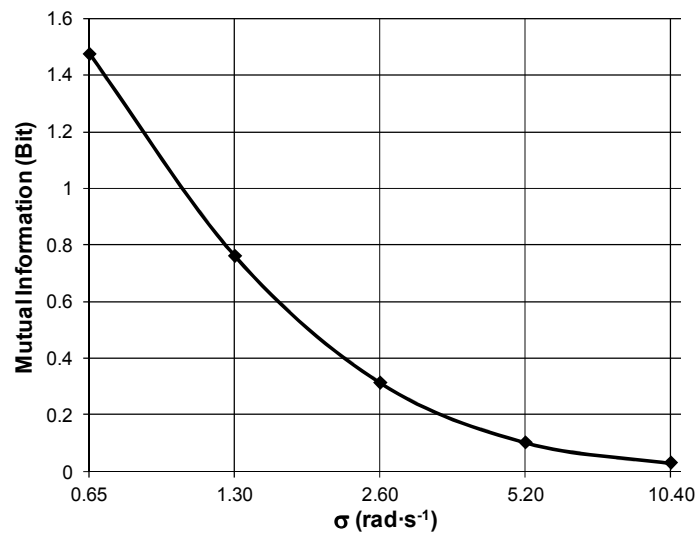


**Fig. 6.** Mutual information in bits between true optic flow and optic flow contaminated with additive Gaussian noise, as a function of the standard deviation of that noise. The abscissa is in log scale; the value 1.308 corresponds to the mean absolute value of the true optic flow over the entire dataset. Mutual information is computed over  $7.68 \cdot 10^6$  joint occurrence data, as was the mutual information between the individual estimators and true optic flow.

Mutual information between all estimators taken singly and true optic flow is surprisingly low. The value for the best, the Basic Lucas-Kanade method, is comparable to that for additive noise contamination with a standard deviation about 1.6 times the mean absolute value of true optic flow; for the EMD estimators, comparable performance corresponds to standard deviations 7 – 8 times mean absolute value.

One particularly intriguing result, however, is that although the mutual information for the EMDs considered singly is quite low, it increases dramatically for the Fourier modes, whereas with the computational algorithms mutual information for the single estimators is much higher but shows a modest increase, or a decrease, when the Fourier modes are considered. This trend is most extreme for the Gradient Method, and examination of its estimates suggests that extreme outlier values in these estimates could be a contributing factor. Such outliers are not present in the outputs of the EMD algorithms due to the bounded nature of the signals at each stage of the processing. While outliers produced by the computational algorithms are infrequent enough to have little effect on the mutual information of the single estimators, they are sufficiently frequent and large enough in magnitude that they could be expected to have a greater impact on the mutual information of the Fourier modes, each of which represents a weighted sum of 384 single estimator outputs. To examine this issue, we recomputed the mutual information for the Fourier modes for the Gradient and Basic Lucas-Kanade algorithms, with outlier values of the individual estimators omitted from each sum (i.e., set to zero). Outliers were defined for this purpose as values greater in magnitude than  $32.725 \text{rad} \cdot \text{s}^{-1}$  (a value that bounds all but 0.0017% of the true optic flow measurements). The results are given in Table 3.

<b>ESTIMATOR (with outlier rejection)</b>	<i>A0</i>	<i>A1</i>	<i>A2</i>	<i>B1</i>	<i>B2<sub>f</sub></i>
Gradient Method	1.40	0.0414	0.0596	0.0502	0.0676
Basic Lucas-Kanade	0.570	0.266	0.459	0.220	0.383

**Table 3.** Mutual information in bits between the spatial Fourier modes of true optic flow and estimators, for the two computational algorithms used in the study, in conjunction with a form of outlier rejection (all estimator values greater in magnitude than  $32.725 \text{rad} \cdot \text{s}^{-1}$  are omitted from the sums).

Interestingly, the performance for dc mode *A0* produced by the Gradient Method is significantly improved by outlier rejection, but the other four modes show little change. This suggests that under the spatiotemporal statistics generated by the closed-loop flight scenario, there is some systematic form of error with this estimator that affects the spatially-weighted sums in the higher order modes, but is reduced in the homogeneously-weighted sum of the dc mode. For Basic Lucas-Kanade, there is only modest improvement for four of the five mode estimates, and a slight degradation for the *B1* mode, suggesting that outliers have a minor effect. While more sophisticated approaches might be useful in reducing ill-conditioned behavior by computational optic flow algorithms, by way of contrast, the bio-inspired algorithms have the inherently favorable property of substantial information gain as the poor optic flow estimates represented by

their individual outputs are summed spatially for WFI control. The benefits realized by this operation presumably also accrue in wide-field neurons, such as the LPTCs, that play a role in the biological optomotor control system.

Also of interest is the fact that the mutual information figures for the ‘Raw EMD’ and the versions with gain control models for motion adaptation are not significantly different. Comparative work (Shoemaker et al., 2005) has shown that such adaptive models significantly reduce variability of EMD responses to various animated natural images – in other words, that they improve the degree of velocity constancy of the EMD. Similarly, experiments with closed-loop WFI control using the estimators in the current study demonstrate that the Raw EMD will not support collision-free travel through unstructured environments with obstructions, whereas the models with motion adaptation, although not absolutely reliable, generally do. These results suggest that the mutual information, while generally informative, is not an ideal predictor of performance with respect to closed-loop local guidance and collision avoidance. More detailed findings regarding closed-loop control, and the development of a metric capable of better predicting closed-loop performance, will be addressed in subsequent publications.

A significant overall conclusion of the study by Shoemaker et al. (2005) is that current elaborated models for EMD-based visual motion detection cannot fully explain the degree of velocity constancy seen in the responses of the LPTCs to moving imagery (Shoemaker et al., 2005; Straw et al., 2008). Such elaborations include gain control-based motion adaptation, as well as the ‘gain control’ that is an inherent consequence of the biophysics of signal integration in the LPTCs (Borst et al., 1995). These results all suggest that, in spite of the favorable spatial integration properties of our bio-inspired algorithms, they are unable to provide the quality of information about optic flow that is available to the fly’s optomotor control system during visually-guided flight. As details of the processing that takes place in insect motion vision become better understood, the performance of models incorporating these details will almost certainly improve, and thus there is hope that they may eventually become a significant component of artificial autonomous systems.

## **Appendix:** Estimation of mutual information

As noted in Section 4, the mutual information M.I.(continuous) between true optic flow and estimator output was estimated by the value M.I.(discrete) obtained from joint and marginal histograms. Several techniques were used to make that estimate as accurate as possible, including multi-resolution histograms, and stepping of histogram resolution in conjunction with bias correction.

For all algorithms except the Gradient Method, two bin resolutions were defined by compiling the marginal distributions for OF and EST each at a fixed bin size, and then choosing for each a central region about the origin, and tail regions, so that 70% of the occurrences fell in the center and 30% in the tails. In subsequent discretizations of each one-dimensional space, half of the bins were allotted (with resulting high resolution) to the central region, and half (with lower resolution) to the tails. A joint histogram with rectangular bins was then constructed based on the discretization for each variable. This histogram contained the square of the number of bins NBIN for each marginal distribution, with a central region having small bin size in both dimensions; four regions

with small bin size in one dimension and large in the other (i.e., in the central region of one random variable and tails of the other); and four regions of large bin size in both dimensions, in the corners of the space. For the Gradient Method, which produced extreme outliers among the estimates, three resolutions were used for the estimator dimension, including very low bin width in the far tails. A fraction of the bins allotted for the tails were assigned to the outlier regions based on the ratio of the number of outliers to non-outliers in the tails. The values for the partition of outliers was set at  $\pm 65.45 \text{rads}^{-1}$ , based on consideration of ‘flybot’ dynamics and inspection of the marginal distributions. This multi-resolution procedure allows capture of finer structure of the joint distribution in regions of highest probability density.

In an iterative procedure, NBIN was incremented and M.I.(discrete) computed for each successive value. Using this procedure to estimate the mutual information M.I.(continuous) allows capture of the structure of the probability space with increasing accuracy as the number of bins increases. However, for any finite sample, it is well known that the histogram-based estimate induces a bias (Herzel and Grosse, 1995; Grosse, 1996) that increases with the number of histogram bins. We developed a procedure based on two estimates of the bias, in order to produce as accurate as possible an estimate of the asymptotic value of the mutual information as the number of histogram bins was increased for the fixed, finite sample size.

Herzel and Grosse (1995) produced an estimate of this bias based on the number of bins  $\text{MBIN}_{\text{joint}}$  in the joint histogram, and numbers of bins  $\text{MBIN}_{\text{OF}}$  and  $\text{MBIN}_{\text{EST}}$  in the marginals, that each contain at least one occurrence:

$$\text{BIAS}_{\text{HG}} = (\text{MBIN}_{\text{joint}} - 2 \cdot \text{MBIN}_{\text{OF}} - 2 \cdot \text{MBIN}_{\text{EST}} + 1) / (2 \cdot N_{\text{D}}),$$

where  $N_{\text{D}}$  is the total number of joint occurrence data. Empirically, we found that  $\text{BIAS}_{\text{HG}}$  underestimates the true bias, as the bias-corrected estimate  $\text{M.I.}(\text{discrete}) - \text{BIAS}_{\text{HG}}$  increases rather than asymptotes at large NBIN. A similar estimate of the bias based on the total number of bins,

$$\text{BIAS}_{\text{A}} = (\text{NBIN}^2 - 4 \cdot \text{NBIN} + 1) / (2 \cdot N_{\text{D}}),$$

was found to consistently overestimate the bias. Therefore, an interpolation between the two was performed:

$$\text{M.I.}(\text{continuous}) \approx \text{M.I.}(\text{discrete}) - b \cdot \text{BIAS}_{\text{A}} - (1-b) \cdot \text{BIAS}_{\text{HG}},$$

where  $b \in (0,1)$  is chosen such that  $\text{M.I.}(\text{discrete})$  assumes the same value at two large values of NBIN, values for which the bias-corrected estimated would be expected to be very near asymptote. For the individual estimators, these values of NBIN were  $2^9$  and  $2^{10}$ , and the number of joint occurrence data  $N_{\text{D}} = 7.68 \cdot 10^6$ . Fig. 7 illustrates  $\text{M.I.}(\text{discrete})$ , the two bias corrections, and the final estimated asymptotic value for the EMD estimator with ‘neural’ gain control.

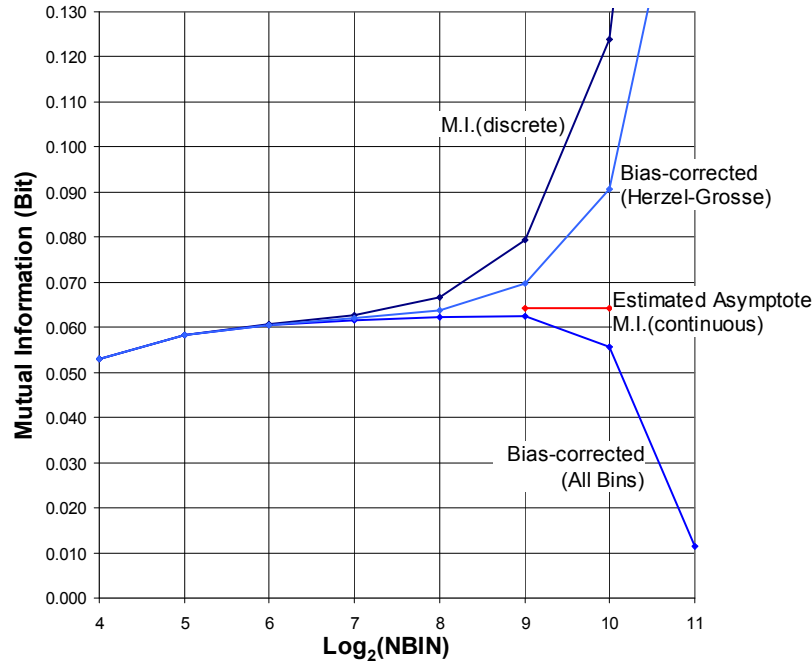


**Fig. 7.** The estimator M.I.(discrete) for the EMD algorithm with ‘neural’ gain control, as a function of the number of bins NBIN per marginal histogram. Bias-corrected values and the interpolated estimate for M.I.(continuous) are also depicted and labeled.

The same approach was taken to estimate the mutual information for each of the Fourier modes  $A0$ ,  $A1$ ,  $A2$ ,  $B1$ , and  $B2_f$ . In these cases, the two values of NBIN chosen for asymptote estimation were 128 and 182, and  $N_D = 2 \cdot 10^4$ .

## Acknowledgments

This work was supported by US Air Force contract FA8651-07-C-0099. The authors thank the anonymous reviewers for helpful comments.

## References

- Adelson EH, Bergen JR (1985) Spatiotemporal energy models for the perception of motion. *Journal of the Optical Society of America A* 2:284-299.
- Barnett PD, Nordström K, O’Carroll D (2010) Motion adaptation and the velocity coding of natural scenes. *Current Biology* 20:994-999.
- Bouguet J-Y (1999) Pyramidal Implementation of the Lucas-Kanade Feature Tracker. OpenCV Documentation, Microprocessor Research Lab, Intel Corporation, Santa Clara, CA.
- Borst A, Haag J (2002) Neural networks in the cockpit of the fly. *Journal of Comparative Physiology A* 188:419-437.
- Borst A, Haag J, Reiff D (2010) Fly motion vision. *Annual Review of Neuroscience* 33:49-70.
- Borst A, Egelhaaf M, Haag J (1995) Mechanisms of dendritic integration underlying gain control in fly motion-sensitive neurons. *Journal of Computational Neuroscience* 2:5-18.
- Clifford CWG, Langley K (1996) A model of temporal adaptation in fly motion vision. *Vision Research* 36:2595-2608.
- Clifford CWG, Ibbotson MR (2003) Fundamental mechanisms of visual motion detection: models, cells and functions. *Progress in Neurobiology* 68:409-437.

- Collett TS, Land MF (1975) Visual control of flight behaviour in the hoverfly, *Syritta pipiens* L. *Journal of Comparative Physiology A* 99:1–66.
- Dahmen HJ, Franz MO, Krapp HG (2001) Extracting egomotion from optic flow: limits of accuracy and neural matched filters. In: Zanker J, Zeil J (eds) *Motion Vision – Computational, Neural and Ecological Constraints*, Springer, Berlin, Heidelberg, New York, pp 143-168.
- Dickson WB, Straw AD, Dickinson MH (2008) Integrative model of *Drosophila* flight. *AIAA Journal* 46:2150-2164.
- Dror RO, O’Carroll DC, Laughlin SB (2001) Accuracy of velocity estimation by Reichardt correlators. *J. Opt. Soc. Am. A* 18:241-252.
- Egelhaaf M, Borst A, Reichardt W (1989) Computational structure of a biological motion-detection system as revealed by local detector analysis in the fly’s nervous system. *Journal of the Optical Society of America A* 6:1070-1087.
- Egelhaaf M, Borst, A (1993) Movement detection in arthropods. In: Miles FA and Wallman J (eds) *Visual Motion in the Stabilization of Gaze*, pp 3-27, Elsevier, Amsterdam.
- Egelhaaf M, Kern R, Krapp HG, Kretzberg J, Kurtz R, Warzecha A (2002) Neural encoding of behaviourally relevant visual-motion information in the fly. *Trends in the Neurosciences* 25:96–102.
- Franceschini N, Riehle A, Le Nestour A (1989) Directionally selective motion detection by insect neurons. In: Stavenga DG and Hardie RC (eds) *Facets of Vision*, pp 360-390, Springer-Verlag, Berlin.
- Franz MO, Krapp HG (2000) Wide-field, motion sensitive neurons and matched filters for optic flow fields. *Biological Cybernetics* 83:185-197.
- Fry SN, Sayaman R, Dickinson MH (2003) The aerodynamics of free flight maneuvers in *Drosophila*. *Science* 300:495-498.
- Grosse I (1996) Estimating entropies from finite samples. In: Freund JA (ed) *Dynamik – Evolution – Strukturen*, Verlag Dr. Köster, Berlin.
- Haag J, Denk W, Borst A (2004) Fly motion vision is based on Reichardt detectors regardless of the signal-to-noise ratio. *Proceedings of the National Academy of Sciences USA* 101:16333-16338.
- Harris RA, O’Carroll DC, Laughlin SB (1999) Adaptation and the temporal filter of fly motion detectors. *Vision Research* 39:2603-2613.
- Harris RA, O’Carroll DC, Laughlin SB (2000) Contrast gain reduction in fly motion adaptation. *Neuron* 28:595-606.
- Hassenstein B, Reichardt W (1956) Systemtheoretische analyse der Zeit-, Reihenfolgen-, und Vorseichenauswertung bei der Berwegungsperzeption des Rüsselkäfers *Chlorophanus*. *Zeitschrift für Naturforschung* 11b:513-524.
- Hausen K (1982a) Motion sensitive interneurons in the optomotor system of the fly. I. The horizontal cells: structure and signals. *Biological Cybernetics* 45:143-156.
- Hausen K (1982b) Motion-sensitive interneurons in the optomotor system of the fly. II. The horizontal cells: Receptive field organization and response characteristics. *Biological Cybernetics* 46:67-79.
- Hausen K, Egelhaaf M (1989) Neural mechanisms of visual course control in insects. In: *Facets of Vision* (Edited by Stavenga DG, Hardie RC). 391-424. Springer Verlag, Berlin
- Herzel H, Grosse I (1995) Measuring correlations in symbols sequences. *Physica A* 216:518–542.
- Hesselberg T, Lehmann FO (2007) Turning behavior depends on frictional damping in the fruit fly *Drosophila*. *Journal of Experimental Biology* 210:4319-4334.
- Humbert JS, Hyslop AM (2010) Bio-inspired visuomotor convergence. *IEEE Transactions on Robotics* 26:121-130.
- Hyslop AM, Krapp HG, Humbert JS (2010) Control theoretic interpretation of directional motion preferences in optic flow processing interneurons. *Biological Cybernetics*, DOI 10.1007/s00422-010-0404-8.
- Kirschfeld K (1991) An optomotor control system with automatic compensation for contrast and texture. *Proceedings of the Royal Society of London B* 246:261-268.
- Koenderink JJ, van Doorn AJ (1987) Facts on optic flow. *Biological Cybernetics* 56: 247-254.
- Krapp HG, Hengstenberg B, Hengstenberg R (1998) Dendritic structure and receptive-field organization of optic flow processing interneurons in the fly. *Journal of Neurophysiology* 79:1902-1917.
- Laughlin SB (1976) Neural integration in the first optic neuropile in dragonflies. IV. Interneuron spectral sensitivity and contrast encoding. *Journal of Comparative Physiology* 112:199-211.
- Laughlin S (1984) The roles of parallel channels in early visual processing by the arthropod compound eye. In Ali MA (ed) *Photoreception and vision in invertebrates*. Plenum Press, New York, pp 457-481.

- Lipetz LE (1971) The relation of physiological and psychological aspects of sensory intensity. In: Loewenstein WR (ed) Handbook of sensory physiology. Springer, Berlin Heidelberg New York, pp 192–225.
- Lucas BD, Kanade T (1981) An iterative image registration technique with an application to stereo vision. Proceedings of the 7th International Joint Conference on Artificial Intelligence, pp 674-679. Vancouver, Canada, 1981.
- Maddess T, Laughlin SB (1985) Adaptation of the motion sensitive neuron H1 is generated locally and governed by contrast frequency. Proc. R. Soc. London B 225:251–275.
- McCarthy C, Barnes N (2004) Performance of optical flow techniques for indoor navigation with a mobile robot. Proceedings of IEEE International Conference on Robots & Automation, pp 5093-5098. New Orleans, LA, 2004.
- Naka KI, Rushton WAH (1966) S-potentials from luminosity units in retina of fish (*Cyprinidae*). Journal of Physiology (London) 185:587-599.
- Reiser MB, Humbert JS, Dunlop MJ, del Vecchio D, Murray RM, Dickinson MH (2004) Vision as a compensatory mechanism for disturbance rejection in upwind flight. Proceedings of American Control Conference 1:311-316.
- Rind FC (1996) Intracellular characterization of neurons in the locust brain signaling impending collision. Journal of Neurophysiology 75:986-995.
- van Santen JPH, Sperling G (1984) Temporal covariance model of human motion perception. Journal of the Optical Society of America 1:451-473.
- Shoemaker PA, O'Carroll DC, Straw AD (2005) Velocity constancy and models for wide-field motion detection in insects. Biological Cybernetics 93:275-287.
- Srinivasan MV, Guy RG (1990) Spectral properties of movement perception in the dronefly *Eristalis*. Journal of Comparative Physiology A 166:287-295.
- Srinivasan MV, Zhang SW, Chandrashekhara K (1993) Evidence for two distinct movement-detecting mechanisms in insect vision. Naturwissenschaften 80:38-41.
- Srinivasan MV, Zhang SW, Lehrer M, Collet TS (1996) Honeybee navigation en route to the goal: visual flight control and odometry. Journal of Experimental Biology 199:237-244.
- Srinivasan M, Zhang SW (2004) Visual motor computations in insects. Annual Review of Neuroscience 27:679–696.
- Straw AD, Rainsford T, O'Carroll D (2008) Contrast sensitivity of insect motion detection to natural images. Journal of Vision 8:1-9.
- Tolhurst DJ, Tadmor Y, Chao T (1992) Amplitude spectra of natural images. Ophthalmology and Physiological Optics 12:229-232.
- Wolf-Oberhollenzer F, Kirschfeld K (1994) Motion sensitivity in the nucleus of the basal optic root of the pigeon. Journal of Neurophysiology 71:1559-1573.